Journal of Catalysis 396 (2021) 179–191

Contents lists available at ScienceDirect

Journal of Catalysis

journal homepage: www.elsevier.com/locate/jcat

Manipulating morphology and surface engineering of spinel cobalt oxides to attain high catalytic performance for propane oxidation

Wenjun Zhu [a,b], Xiao Chen [a], Chuang Li [a], Zhongmin Liu [b,*], Changhai Liang [a,*]

[a] State Key Laboratory of Fine Chemicals & Laboratory of Advanced Materials and Catalytic Engineering, Dalian University of Technology, Dalian 116024, China
[b] National Engineering Laboratory for Methanol to Olefins, Dalian National Laboratory for Clean Energy, Dalian Institute of Chemical Physics, Chinese Academy of Sciences, Dalian 116023, China

ARTICLE INFO

Article history:
Received 23 December 2020
Revised 1 February 2021
Accepted 15 February 2021
Available online 24 February 2021

Keywords:
Propane oxidation
Morphologies
Water vapor resistance
Co_3O_4
Volatile organic compounds

ABSTRACT

The selective synthesis of nanomaterials with different morphologies and crystal facets is of great significance for catalytic properties and practical applications. We report a strategy for controllable fabrication of hierarchical Co_3O_4 materials with various morphologies (ellipsoidal, flowerlike, book-shaped, spindle-like) and study their catalytic properties in propane oxidation. Co_3O_4-B (book-shaped) is found to exhibit the highest propane oxidation rate (0.86×10^{-8} mol m^{-2} s^{-1}) and the highest turnover frequency (TOF = 11.49×10^{-3} s^{-1}) at 220 °C. This confirms that Co_3O_4-B provides a higher specific surface area, a highly exposed {1 1 0} facet, and abundant Co^{3+} cations, which make it exhibit favorable low-temperature reducibility and oxygen mobility and thus improve its catalytic activity. In situ diffuse reflectance infrared Fourier transform spectroscopic analysis reveals that the intermediates, such as carboxylate and carbonate species, are involved in propane oxidation. Furthermore, Co_3O_4-B shows high water-resistance performance, and no significant deactivation is observed after long-term stability and reusability tests.

1. Introduction

Rapid urbanization and industrialization give rise to an increase in volatile organic compound (VOC) emissions, which are considered major contributors to environmental pollution and are hazardous to human health. The effective elimination of VOCs has been extensively investigated in the past few decades [1]. Compared with other techniques (e.g., adsorption [2], photocatalysis [3], and plasma [4]) for VOC elimination, catalytic oxidation is generally assumed to be one of the most efficient techniques, owing to its advantages of high efficiency, low operating temperature, and harmless products [5,6]. The design of highly efficient and stable catalysts is a key factor in catalytic oxidation. Catalysts based on noble metals (Pt [7,8], Pd [9,10], Au [11], etc.) always exhibit outstanding catalytic properties at relative low temperatures. However, their general application is severely hindered due to high cost, easy sintering, and susceptibly to poisoning in the presence of sulfur compounds or water.

Great efforts have been made in the design of transitional metal oxides as alternatives for traditional noble metal catalysts. It is generally accepted that a higher specific surface area with rich valence metal ions and more structure defects would make a difference to the catalytic performance of transitional metal oxides, including low-temperature reducibility, oxygen vacancies, and mobility [12]. However, how to achieve and adjust catalytic materials with enhanced catalytic performance still remains a great challenge. According to experimental and theoretical results, there is a certain relationship between the shape and the properties of the catalyst, and the catalytic activity is strongly dependent on its morphology [13–16]. Therefore, the design and controlled synthesis of transition metal oxide catalysts is significant for achieving catalytic activity equivalent to that of noble metal catalysts.

As typical transition-metal oxides, cobalt oxides exhibit remarkable catalytic performance in a variety of catalytic reactions, such as CO oxidation [12], N_2O decomposition [17], and hazardous VOC catalytic oxidation [18,19] due to its good redox properties, high oxygen mobility, and facile generation of active oxygen species [20,21]. Furthermore, a number of works have reported that Co_3O_4 catalysts with the same composition exhibit different catalytic activity due to their diverse shapes, crystal planes, specific surface areas, active species, and reducibility [22–25]. For example, Hu et al. found that Co_3O_4 nanosheets with a predominant exposed {1 1 2} plane were more active for methane combustion than Co_3O_4 nanobelts ({0 1 1} facets) and nanocubes ({0 0 1} facets) [26]. Xie et al. found that Co_3O_4 nanorods with highly exposed {1 1 0} planes favored the existence of active Co^{3+} species on the surface and exhibited superior catalytic activity

* Corresponding authors.
E-mail addresses: liuzm@dicp.ac.cn (Z. Liu), changhai@dlut.edu.cn (C. Liang).

https://doi.org/10.1016/j.jcat.2021.02.014
0021-9517/

for CO oxidation [27]. Ren et al. investigated 3D hierarchical Co_3O_4 nanomaterials for toluene oxidation and found that cube-stacked Co_3O_4 microsphere material with highly exposed {1 1 0} facets, abundant high-valence Co ions, and surface-adsorbed oxygen species exhibited the highest catalytic activity [28]. As a result, the selective synthesis of nanostructured Co_3O_4 catalysts with different morphologies and highly exposed crystal facets is of great significance to the catalyst properties and practical applications.

However, overall comprehension of the role of the morphologies and exposed crystal facets of Co_3O_4 catalysts in propane oxidation is in its infancy. Here, we report a strategy for the controllable fabrication of hierarchical nanostructure Co_3O_4 materials with different morphologies and applying them to propane oxidation. Various characterization methods such as X-ray diffraction (XRD), N_2 adsorption/desorption, scanning electron microscopy (SEM), transmission electron microscopy (TEM)/high-resolution TEM (HRTEM), H_2 temperature-programmed reduction (H_2-TPR), O_2 temperature-programmed desorption (O_2-TPD), C_3H_8-TPD, C_3H_8 temperature-programmed surface reaction (C_3H_8-TPSR)/(C_3H_8-TPSR-H), and in situ diffuse reflectance infrared Fourier transform spectroscopy (in situ DRIFTS) were employed to study the crystal structure, morphologies, and surface chemical properties of the synthesized Co_3O_4 samples and to investigate their correlation with catalytic performance systematically. Furthermore, the influence of water vapor on catalytic activity and stability over the Co_3O_4 catalysts with different morphologies was explored, and a possible catalytic propane oxidation mechanism on Co_3O_4 catalysts was proposed.

2. Experimental

2.1. Catalyst preparation

All chemicals were analytical reagent grade and could be used directly for experiments without further treatment. The samples were synthesized by hydrothermal strategies, where the fabrication of ellipsoidal Co_3O_4 nanomaterials and spindlelike Co_3O_4 nanomaterials was slightly modified according to a previous study [28].

2.1.1. Synthesis of hierarchical ellipsoidal Co_3O_4 nanomaterials (Co_3O_4-E)

$Co(CH_3COO)_2{\cdot}4H_2O$ (15 mmol) was dissolved in 70 mL of ethylene glycol at room temperature (RT). Subsequently, urea (30 mmol) was added to the solution with vigorous stirring for 1 h. Then the obtained solution was poured into a 100 mL Teflon-lined stainless steel autoclave, sealed, and kept at 180 °C for 12 h. After being naturally cooled down to RT, the powder was acquired by centrifugation and washed thoroughly with ethanol and deionized water. Finally, the obtained powder was dried overnight at 80 °C and calcined in air from RT to 350 °C for 3 h (1 °C min^{-1}).

2.1.2. Synthesis of hierarchical flowerlike Co_3O_4 nanomaterials (Co_3O_4-F)

The synthesis procedure was similar to that of Co_3O_4-E, except for the precursors and hydrothermal temperature: $Co(CH_3COO)_2{\cdot}4H_2O$ (8 mmol), 70 mL of methanol, polyvinyl pyrrolidone (0.15 g PVP) at 190 °C for 12 h.

2.1.3. Synthesis of hierarchical spindlelike Co_3O_4 nanomaterials (Co_3O_4-S)

The synthesis procedure was similar to that of Co_3O_4-E, except for the precursors and hydrothermal temperature: $CoCl_2{\cdot}6H_2O$ (15 mmol), 70 mL of deionized water, urea (75 mmol) at 100 °C for 12 h.

2.1.4. Synthesis of hierarchical book-shaped Co_3O_4 nanomaterials (Co_3O_4-B).

The synthesis procedure was similar to that of Co_3O_4-E, except for the precursors and hydrothermal temperature: $Co(NO_3)_2{\cdot}6H_2O$ (15 mmol), 70 mL of deionized water, urea (75 mmol) at 100 °C for 12 h.

2.2. Catalyst characterization

Powder XRD measurements were conducted on a SmartLab 9KW diffractometer using CuKα radiation. The N_2 adsorption–desorption isotherms were obtained at −196 °C on a Quantachrome Autosorb-iQ instrument. Prior to each measurement, the samples were outgassed at 200 °C for 10 h. The morphologies and microstructures of catalysts were analyzed by SEM (FEI Nova NanoSEM 450) and TEM (FEI Tecnai G20 F30 S-TWIN). XPS measurements were carried out on a Thermo ESCALAB 250 electron spectrometer with an Al$K\alpha$ ($h\nu$ = 1486.8 eV) excitation source.

H_2-TPR and O_2-TPD experiments were conducted on a Micromeritics Autochem II 2920 chemisorption analyzer. For H_2-TPR, 50 mg of catalyst was pretreated in an Ar stream (30 mL min^{-1}) at 200 °C for 1 h. Then the H_2-TPR experiment was programmed for heating to 600 °C (10 °C min^{-1}) in a 10 vol% H_2/Ar flow (30 mL min^{-1}). For O_2-TPD, 100 mg of catalyst was pretreated in 10 vol% O_2/He flow (30 mL min^{-1}) at 300 °C for 30 min. Then the samples were swept with a He flow (30 mL min^{-1}) at 50 °C for 1 h. The O_2-TPD experiment was programmed for 600 °C (10 °C min^{-1}) in a He flow (30 mL min^{-1}).

C_3H_8-TPD and C_3H_8-TPSR/C_3H_8-TPSR-H (humid conditions) experiments were carried out on a quartz reactor connected to a mass spectrograph (GSD 320 OMNISTAR). For the C_3H_8-TPD experiment, the sample (50 mg) was pretreated at 300 °C for 30 min in an O_2/Ar stream (30 mL min^{-1}). Then the catalyst was exposed to 5 vol% C_3H_8/Ar (40 mL min^{-1}) at 50 °C for 1 h, followed by purging with Ar for 15 min. Finally, the experiment run started from 50 to 350 °C (10 °C min^{-1}) under a gas flow of Ar (40 mL min^{-1}). Noting that C_3H_8 and CO_2 have the same mass, the MS signal of m/z = 43 is used to detect C_3H_8, and CO_2 is obtained using the signal of m/z = 44, subtracting that of m/z = 43. Other MS signals of H_2 (m/z = 2), H_2O (m/z = 18) and CO (m/z = 28) were also recorded by an online MS. C_3H_8-TPSR/C_3H_8-TPSR-H was conducted with a procedure similar to that for C_3H_8-TPD, except for the introduction of 5 vol% O_2/Ar (40 mL min^{-1}) or 0.6 vol% H_2O + 5 vol% O_2/Ar (40 mL min^{-1}) during the heating process.

In situ DRIFTS experiments were conducted using an FTIR spectrometer (Thermo Fisher Nicolet iS50) with an MCT/A detector and a Harrick in situ cell. The sample (40 mg) was pretreated at 300 °C for 1 h in a gas flow of 10 vol% O_2/Ar (50 mL min^{-1}). The background spectra were recorded at certain temperatures. The spectra of C_3H_8 adsorption were recorded under an 0.2 vol% C_3H_8/Ar (50 mL min^{-1}) at 50 °C, and the spectra of C_3H_8 oxidation were obtained with 0.2 vol% C_3H_8, 5 vol% O_2, and balance Ar (50 mL min^{-1}) at 50–300 °C. All spectra were recorded with 64 scans at a resolution of 4 cm^{-1}.

2.3. Catalytic activity evaluation

The catalytic performance of the Co_3O_4 catalysts for propane oxidation was evaluated in a fixed-bed reactor at atmospheric pressure. To eliminate the hot spots effect, the catalyst (100 mg) was diluted in 2 mL of quartz sand (60–80 mesh) and then was placed in a stainless steel tubular reactor. The reactant gas was composed of 0.2 vol% C_3H_8, 5 vol% O_2 (or 5 vol% O_2, 2.5 vol% H_2O), and Ar balance, with a total flow rate of 200 mL min^{-1}, corresponding to a GHSV of 120,000 mL $g^{-1}h^{-1}$. The quantitative analysis of reactant gas and products was performed online by a gas

chromatograph (GC 7900) equipped with FID and TCD detectors. The propane conversion (X_p), CO_2 yield (Y_{CO2}), and specific surface activity (SSA) were calculated as

$$X_p = \frac{C_{p,in} - C_{p,out}}{C_{p,in}} \times 100\%, \quad (1)$$

$$Y_{co_2} = \frac{C_{CO_2}}{C^*_{CO_2}} \times 100\%, \quad (2)$$

$$SSA = \frac{FX_p}{m_{Co}S_{BET}}, \quad (3)$$

where $C_{p,in}$, $C_{p,out}$, C_{CO2}, and C_{CO2}^* are the inlet and outlet propane concentration, the outlet CO_2 concentration, and the CO_2 concentration after 100% propane conversion, respectively. F is the propane flow rate (mol s^{-1}), m_{Co} is the mass of cobalt oxide in the reactor (g), and S_{BET} represents the specific surface area (m^2 g^{-1}). T_{10}, T_{50}, and T_{90} are the temperatures for 10, 50, and 90% propane conversion, respectively.

Turnover frequency (TOF), defined as the number of propane molecules converted per active site per second, is calculated using the oxygen pulse chemisorption according to the literature [29–32],

$$TOF = \frac{FX_p}{2m_{Co}V_{O_2}}, \quad (4)$$

where F is the propane flow rate (mol s^{-1}), X_p is the conversion of propane (<15%), m_{Co} is the mass of the cobalt oxide (g), and V_{O_2} is the O_2 uptake of the catalysts (μmol g^{-1}, as shown in Fig. S1 in the Supporting Information). In addition, the mass diffusion transport limitation was checked by the Weisz–Prater parameter according to the method reported in [33],

$$N_{W-P} = \frac{-r_A\rho_c R^2}{C_{As}D_e} < 1, \quad (5)$$

where $-r_A$ is the observed reaction rate (mol kg^{-1} s^{-1}), ρ_c is the catalyst density (kg m^{-3}), R is the catalyst particle radius (m), D_e is the effective diffusivity (m^2 s^{-1}), and C_{As} is the reactant concentration at the external surface of the catalyst (mol m^{-3}). The calculated value of N_{W-P} at a GHSV of 240,000 mL $g^{-1}h^{-1}$ is 3.97 × 10^{-3}, which implies that the mass transfer limitation can be ignored in this case.

3. Results and discussion

3.1. Morphology and textural properties

Hierarchical nanostructured Co_3O_4 materials with different morphologies (ellipsoidal, flowerlike, book-shaped, spindlelike) are successfully synthesized via hydrothermal methods. The micromorphology of the synthesized Co_3O_4 samples is characterized by SEM. As shown in Fig. 1a and e, the obtained Co_3O_4-E sample presents a uniform elliptic sphere with a size of ca. 5 μm. The detailed observation in the top right corner inset of Fig. 1e shows that the spherical particles could be considered as the self-assembly of aggregated porous Co_3O_4 cubes. From Fig. 1b and f, it can be seen that Co_3O_4-F nanomaterial is fabricated by closely packed nanosheets, presenting a flowerlike microsphere structure with a size of ca. 2.5 μm. Fig. 1c and g show that the Co_3O_4-S sample presents a needle-stacked spindlelike structure, and the length of the needles is identified to be approximately 10 μm. The Co_3O_4-B sample is a book-shaped structure composed of stacked rectangular nanosheets and the dimension is ca. 5 μm (Fig. 1d and h). Moreover, Fig. 1i–l depict schematic diagrams of the Co_3O_4-E, Co_3O_4-F, Co_3O_4-S, and Co_3O_4-B samples, respectively. In short, the morphologies of the synthesized Co_3O_4 samples could be tuned by simply adjusting the precursors and synthesis temperatures.

The XRD patterns of the synthesized Co_3O_4 samples are shown in Fig. 2. Obviously, all Co_3O_4 samples exhibit similar positions and relative intensities of the main diffraction peaks. The diffraction peaks at 19.0°, 31.3°, 36.9°, 38.5°, 44.8°, 55.7°, 59.4°, and 65.2° belong to the (111), (220), (311), (222), (400), (422), (511), and (440) crystal planes of the spinel Co_3O_4 (PDF#42–1467), respectively. In addition, the presence of sharp and symmetric diffraction peaks, as well as the absence of any extra peaks of impurities, indicates the good crystallinity and purity characteristics of the synthesized Co_3O_4 samples. Moreover, the crystallite sizes of Co_3O_4-E, Co_3O_4-F, and Co_3O_4-B samples calculated by the Scherrer equation are relatively similar, in the range of 19–21 nm, while the Co_3O_4-S sample has the largest crystallite size, 30 nm, which is probably attributable to the differences of their morphologies and crystallization temperatures.

N_2 adsorption–desorption isotherms and pore-size distributions of the Co_3O_4 samples are shown in Fig. S2. Obviously, all Co_3O_4 samples display a type Ⅳ isotherm with an H3 hysteresis loop, suggesting the existence of a mesoporous characteristic in all Co_3O_4 samples. The textural properties of these samples in terms of pore volume, average pore size, and specific surface area are listed in Table 1. The average pore size and pore volume of all Co_3O_4 samples are in the range of 2.3–3.3 nm and 0.20–0.24 cm^3 g^{-1}, respectively. Moreover, the specific surface areas of the Co_3O_4-E, Co_3O_4-F, and Co_3O_4-S samples are approximately 37 m^2 g^{-1}, which are lower than that of the Co_3O_4-B sample (46 m^2 g^{-1}). The morphologies and crystallite sizes may account for the differences in specific surface area.

To acquire a deep understanding of the structure and predominantly exposed crystal facet of the synthesized Co_3O_4 samples, TEM and HRTEM characterizations of these samples were performed (Fig. 3). As shown in Fig. 3a, the Co_3O_4-E sample displays a black ellipse with a rough surface. (−202) and (0–22) crystal planes with a lattice spacing of 0.281 nm can be observed in Fig. 3c, and the interfacial angle between them is 60°. The bright dot arrays in the corresponding FFT images (Fig. 3d) are indexed to the [111] zone axis. Therefore, the dominantly exposed facet of Co_3O_4-E is the {111} facet [22,24,28]. For the Co_3O_4-F sample, a tiny separation of the Co_3O_4 hexagonal nanosheet can be observed in Fig. 3e, which reveals that the flowerlike Co_3O_4 microsphere is probably assembled from hexagonal nanosheets serving as constitutive blocks. The (2–20) plane with a lattice spacing of 0.281 nm perpendicular to the (11–1) plane with a lattice spacing of 0.461 nm (Fig. 3g, h) suggests that the mainly exposed facet of Co_3O_4-F is {112} facet [22,23,26,28,34]. Fig. 3i displays that the Co_3O_4-S sample is composed of independent Co_3O_4 needles with a width of approximately 200 nm. The HRTEM image in Fig. 3k shows the (1–13) and (2–20) crystal planes with lattice fringe spaces of 0.243 and 0.281 nm, respectively, and an interfacial angle of 64.9°, which confirms that the predominantly exposed facet of the Co_3O_4-S is the {110} facet [22,28]. Fig. 3m–p show the TEM and HRTEM images of the book-shaped Co_3O_4-B sample. The lattice fringe spaces of 0.243 and 0.238 nm correspond to the (3–11) and (22–2) crystal planes, respectively. Moreover, an interfacial angle of 83.7° between the (3–11) and (22–2) planes can be observed. Therefore, the primarily exposed facet of the Co_3O_4-B is the {011} facet [22,23,26,34].

3.2. Chemical states and redox properties

The surface element composition and chemical state of the synthesized Co_3O_4 samples were studied by XPS. As shown in Fig. 4a, the Co2p XPS spectra of the Co_3O_4 samples show two major peaks at 780.0 and 795.0 eV, which are assigned to the typical Co2$p_{3/2}$

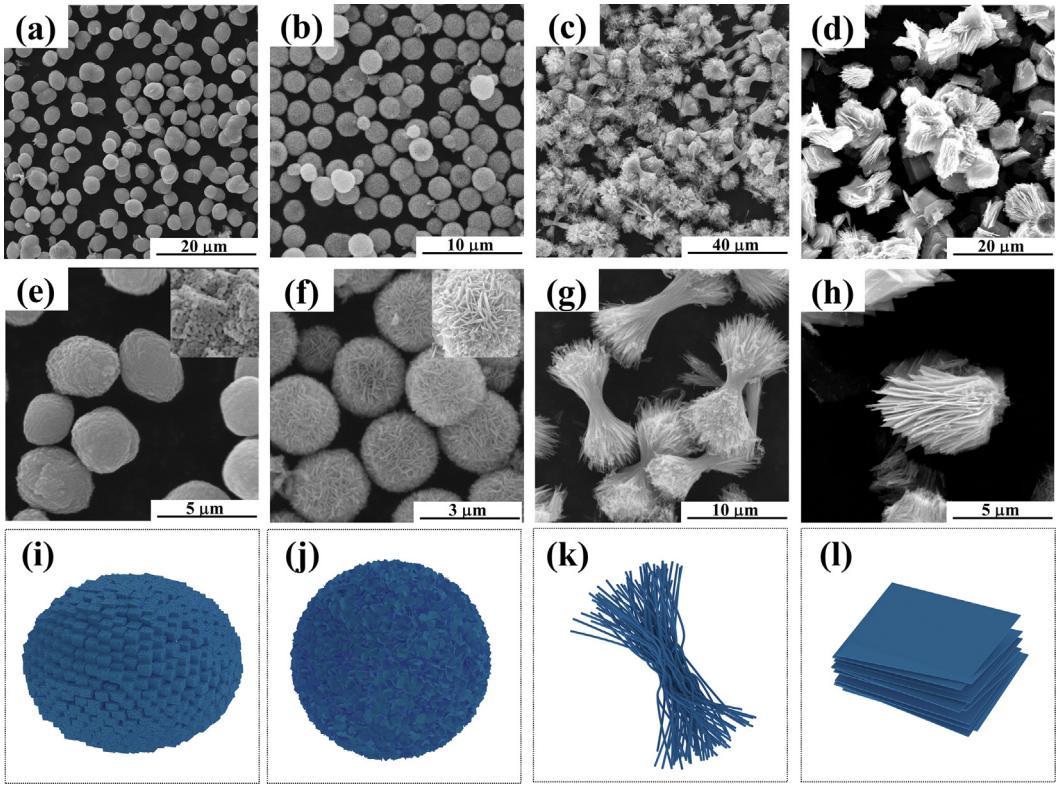

Fig. 1. SEM and schematic images of the synthesized Co_3O_4 samples, Co_3O_4-E (a, e, i), Co_3O_4-F (b, f, j), Co_3O_4-S (c, g, k), and Co_3O_4-B (d, h, l).

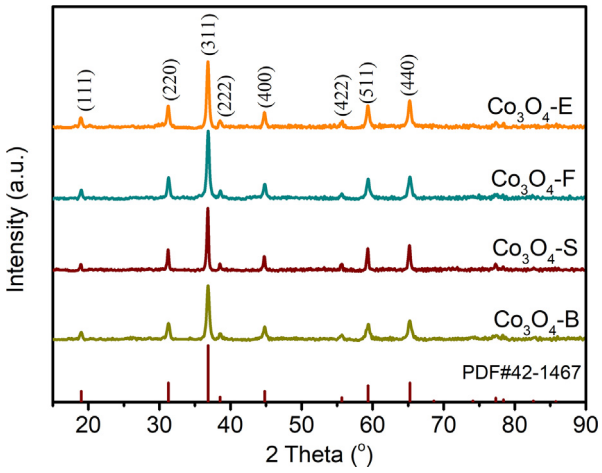

Fig. 2. XRD patterns of the synthesized Co_3O_4 samples.

and Co2$p_{1/2}$ orbitals. Meanwhile, the peaks of Co2$p_{3/2}$ and Co2$p_{1/2}$ can be deconvoluted into four component peaks, where the peaks at 781.5 eV and 797.1 eV belong to Co^{2+} cations, and the peaks at 779.5 eV and 794.8 eV are assigned to Co^{3+} cations. It is reported that the chemical state of the Co components plays a crucial role in the catalytic properties of Co-based catalysts [35], and thus the quantitative analysis of Co valence state is of great significance. The surface Co^{3+}/Co^{2+} atomic ratios of the synthesized Co_3O_4 samples estimated based on the XPS data are listed in Table 1. The results reveal that the surface Co^{3+} amounts of these four samples are different and decrease in the order Co_3O_4-B (0.98) > Co_3O_4-F (0.89) > Co_3O_4-E (0.74) > Co_3O_4-S (0.70). The morphologies synthesized under different conditions affect the surface chemical state (Co^{3+}/Co^{2+}) of the Co_3O_4 samples. Moreover, it can be inferred that Co_3O_4-B sample possesses more Co^{3+} species on the surface, which means that Co_3O_4-B may exhibit superior catalytic performance in propane oxidation.

The O1*s* XPS spectra of the synthesized Co_3O_4 samples are shown in Fig. 4b. Each sample displays an asymmetrical peak, which can be deconvoluted into three component peaks at binding energies of 529.9, 531.0, and 532.9 eV, corresponding to surface lattice oxygen (O_{latt}), surface adsorbed oxygen (O_{ads}), and surface hydroxyl species/water molecules (O_w), respectively [36]. According to the quantitative analysis of the XPS spectra, the O_{ads}/O_{latt}

Table 1
Textural properties and chemical states of the synthesized Co_3O_4 samples.

Sample	D (nm)[a]	S_{BET} ($m^2\ g^{-1}$)[b]	V ($cm^3\ g^{-1}$)[b]	A (nm)[b]	Co^{3+}/Co^{2+} [c]	O_{ads}/O_{latt} [c]
Co_3O_4-E	21	37	0.20	2.9	0.74	0.35
Co_3O_4-F	21	36	0.24	2.3	0.89	0.39
Co_3O_4-S	30	36	0.22	3.3	0.70	0.35
Co_3O_4-B	19	46	0.23	3.1	0.98	0.45

[a] Crystallite sizes calculated from the line broadening of (3 1 1) plane of Co_3O_4.
[b] Specific surface area, pore volume, and average pore size are determined from N_2 adsorption/desorption isotherms.
[c] Data determined from XPS results.

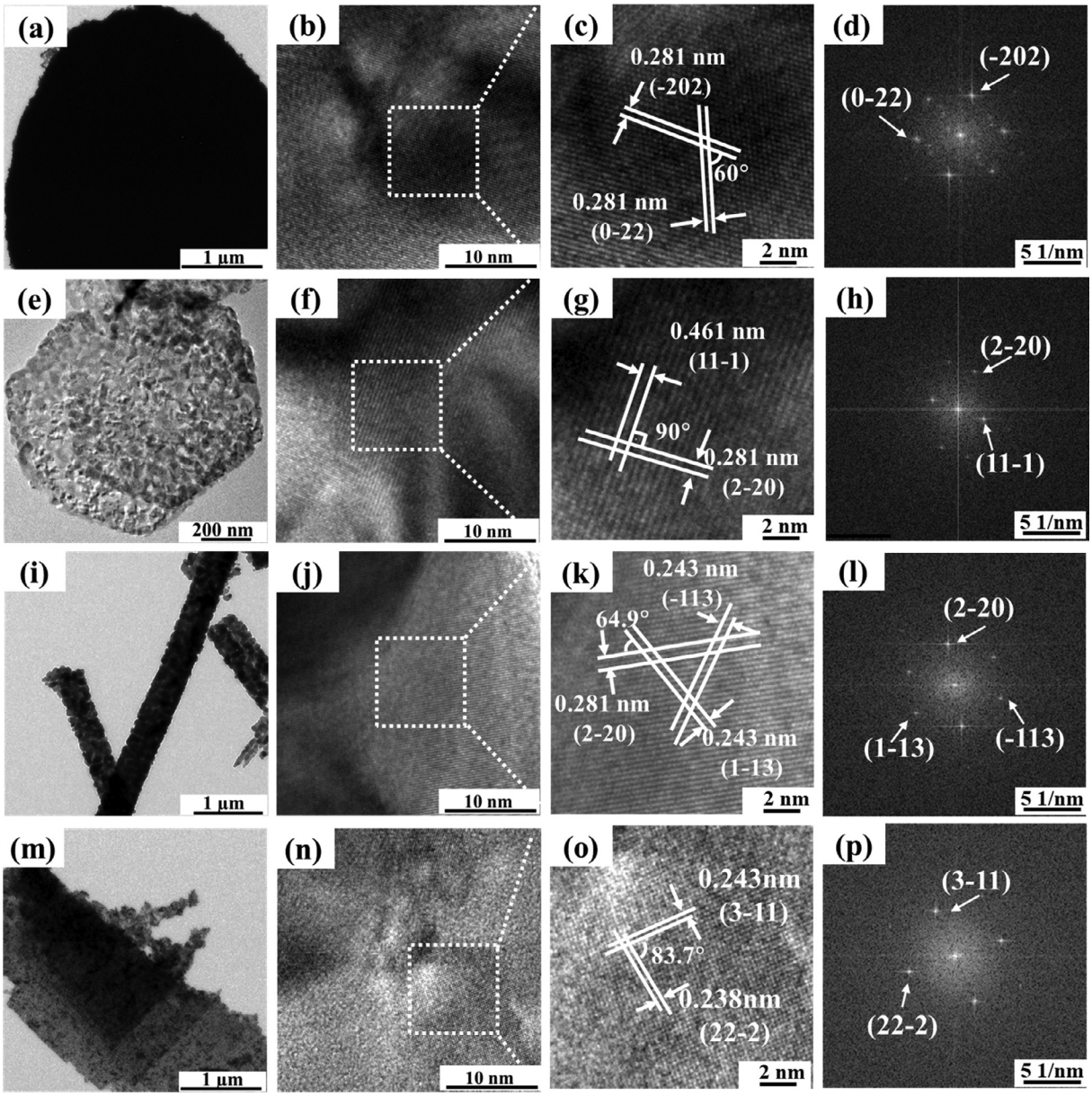

Fig. 3. TEM images of the synthesized Co_3O_4 samples: Co_3O_4-E (a–d), Co_3O_4-F (e–h), Co_3O_4-S (i–l), and Co_3O_4-B (m–p).

atomic ratios vary in the sequence Co_3O_4-B (0.45) > Co_3O_4-F (0.39) > Co_3O_4-E (0.35) > Co_3O_4-S (0.35), demonstrating that there are more O_{ads} species on the Co_3O_4-B surface. Meanwhile, a larger amount of active oxygen species generally implies more oxygen vacancies, which can adsorb and activate gas-phase oxygen to improve the catalytic activity for the oxidation reaction [37,38]. Therefore, higher adsorbed active oxygen species on the Co_3O_4-B sample may give rise to enhanced catalytic performance for propane oxidation.

An H_2-TPR experiment was carried out to investigate the redox properties of the synthesized Co_3O_4 samples, as shown in Fig. 5a. The reduction profiles essentially take on two reduction processes for all Co_3O_4 samples, which correspond to the stepwise reduction of Co^{3+} to Co^{2+} and Co^{2+} to metallic Co. Specifically, the Co_3O_4-B sample has three reduction peaks at 280, 325, and 390 °C. The first reduction peak at 280 °C belongs to the reduction process of Co^{3+} to Co^{2+}, whereas the other two peaks at 325 and 390 °C are assigned to the subsequent reduction of Co^{2+} to metallic Co [25,39]. The reduction behavior of the Co_3O_4 samples strongly depends on their morphology. According to Fig. 5a, the reduction peak at 280 °C for Co_3O_4-B sample is higher than that of other samples, indicating that the Co_3O_4-B sample possesses the largest number of Co^{3+} ions, in accordance with the Co2*p* XPS result. Furthermore, Co_3O_4-E and Co_3O_4-S samples exhibit reduction peaks at 300–310 °C, and the Co_3O_4-F sample shows a slightly lower peak temperature at 288 °C. This confirms the good reducibility of the Co_3O_4-B sample due to its having the lowest reduction peak temperature at 280 °C. All these findings demonstrate that the low-temperature reducibility is particularly enhanced for the Co_3O_4-B sample.

To investigate the oxygen mobility of various oxygen species on the synthesized Co_3O_4 samples, an O_2-TPD experiment was performed and is illustrated in Fig. 5b. Generally, the adsorbed oxygen species change in the following sequence: O_2 (ad) → O_2^- (ad) → O^- (ad) → O^{2-} (latt) [20,40]. According to the curves of synthesized Co_3O_4 samples, three types of oxygen species are observed in the ranges 80–120 and 120–400 °C and above 400 °C, which can be assigned to the desorption of molecular oxygen (O_2), adsorbed oxygen species (O_2^-, O^-), and lattice oxygen species (O^{2-}), respectively.

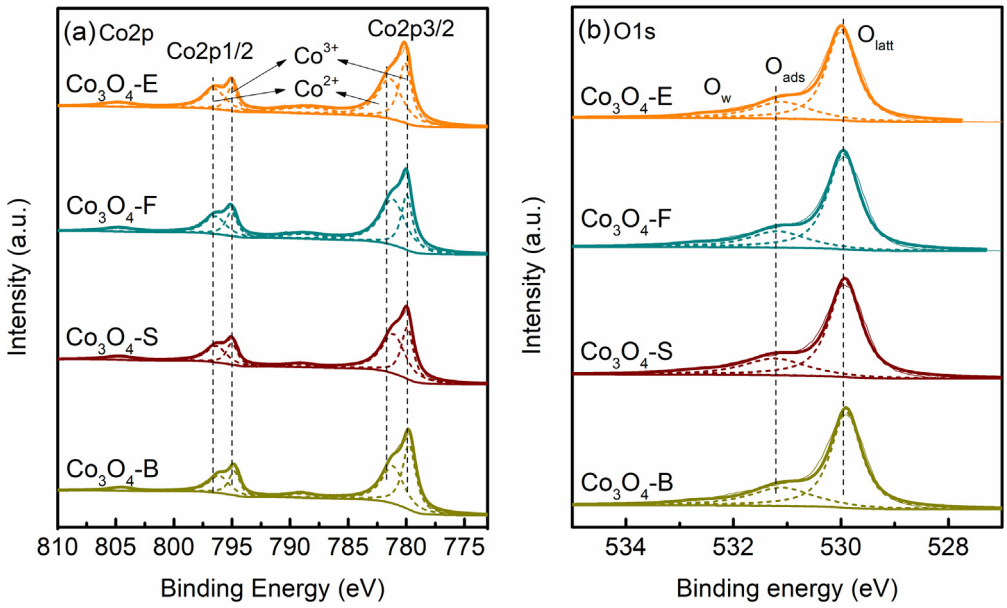

Fig. 4. (a) Co2*p* and (b) O1*s* XPS spectra of the synthesized Co_3O_4 samples.

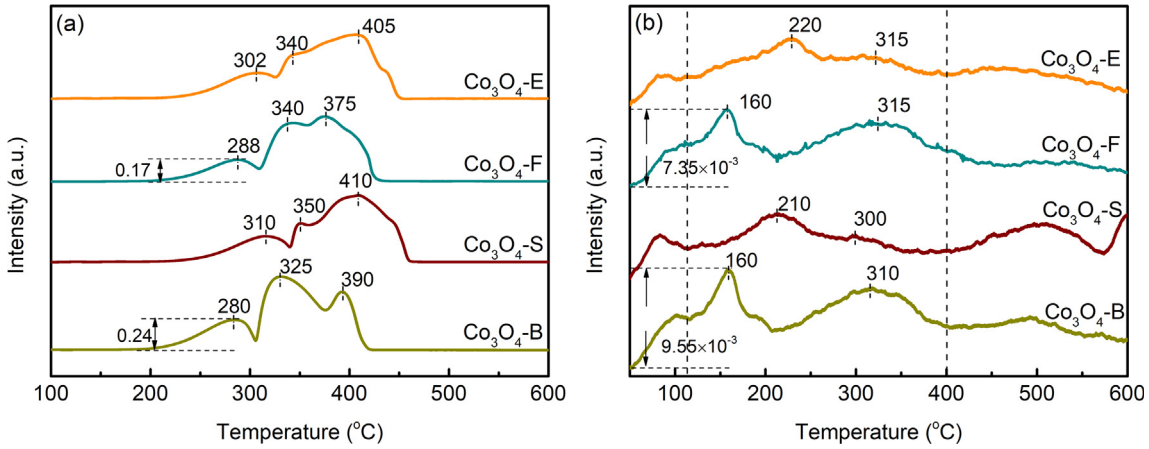

Fig. 5. (a) H_2-TPR and (b) O_2-TPD profiles of the synthesized Co_3O_4 samples.

Apparently, the Co_3O_4-B sample shows larger desorption peaks and lower peak temperatures (160 and 300 °C) in the range of 120–400 °C, indicating the possession of abundant active oxygen species. Therefore, the O_2-TPD result suggests that the Co_3O_4-B sample has abundant active oxygen species and better oxygen mobility, which could be beneficial for propane oxidation.

C_3H_8-TPD experiments were carried out to determine the desorption behavior of propane, and the subsequent C_3H_8-TPSR experiments are used to explore the reactivity of the preadsorbed propane on the catalyst surface. As shown in Fig. 6a, the peaks of CO_2 (m/z = 44) and H_2O (m/z = 18) gradually appear with increasing temperature, whereas the desorption peaks of CO (m/z = 28) and H_2 (m/z = 2) are negligible during the C_3H_8-TPD process over the Co_3O_4-B sample. It can be inferred that either a surface oxygen species or a lattice oxygen species is involved in the propane oxidation reaction. Furthermore, the C_3H_8 desorption behavior of the synthesized Co_3O_4 samples varies with the morphology. Fig. 6b shows the CO_2 production signal of the synthesized Co_3O_4 samples in the C_3H_8-TPD process. Obviously, a larger amount of CO_2 production and a lower peak temperature are observed for the Co_3O_4-B sample, indicating that Co_3O_4-B possesses stronger oxidizing ability for propane than that of other Co_3O_4 samples.

During the C_3H_8-TPSR process (as shown in Fig. 6c), the profile of the Co_3O_4-B sample is similar to that of the C_3H_8-TPD process, where only CO_2 and H_2O peaks exist in the tested temperature range, suggesting that the occurrence of total propane oxidation. However, compared with the C_3H_8-TPD process, a larger amount of CO_2 production is detected in the range 50–340 °C for the C_3H_8-TPSR process, and the CO_2 peak temperature decreases from 220 to 207 °C in the presence of O_2. This confirms that oxygen-containing feed gas accelerates the supplementation of active oxygen species on the catalyst surface, and thus contributes to easier occurrence of propane oxidation. Moreover, the amount of CO_2 production (Fig. 6d) over the synthesized Co_3O_4 catalysts during the C_3H_8-TPSR process follows the order Co_3O_4-B > Co_3O_4-F > Co_3O_4-E > Co_3O_4-S, consistent with the C_3H_8-TPD process. Combined with the O_2-TPD and XPS results, it is reasonable to conclude that the larger amounts of Co^{3+} and active oxygen species of Co_3O_4-B facilitate the adsorption and activation of propane on the catalyst surface.

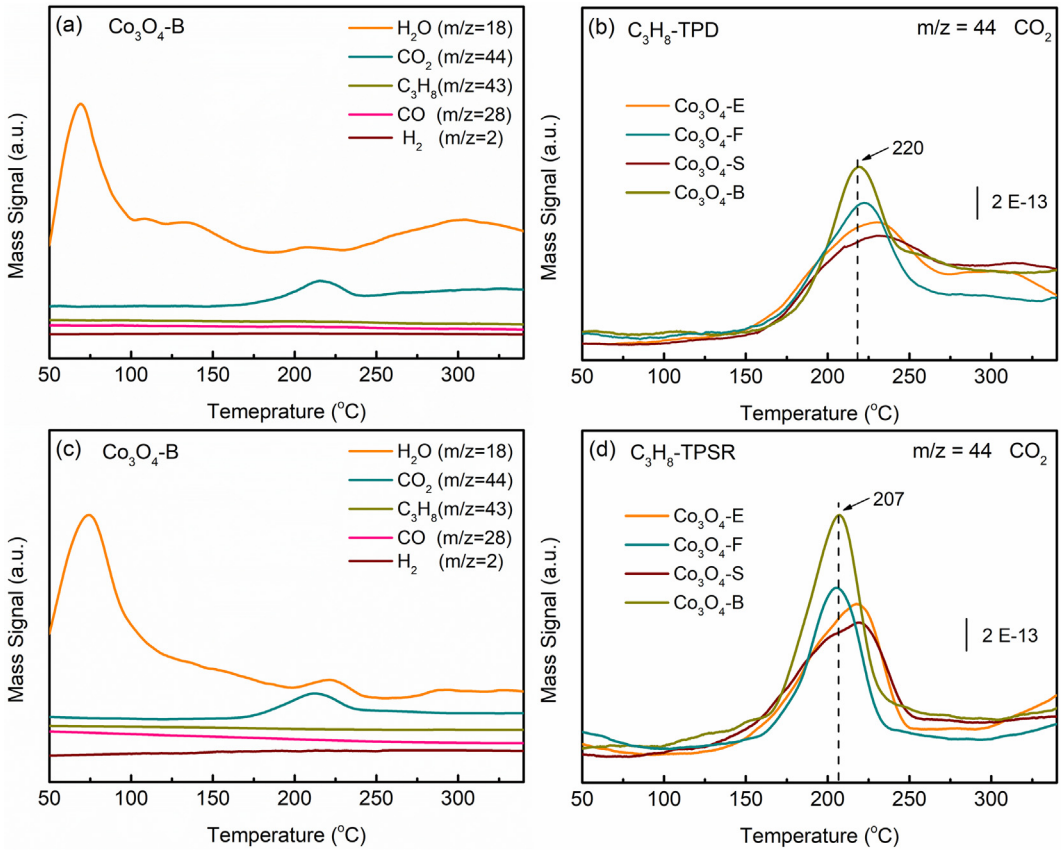

Fig. 6. (a) C_3H_8-TPD profiles of the Co_3O_4-B sample, (b) CO_2 signal of the synthesized Co_3O_4 samples in the C_3H_8-TPD process, (c) C_3H_8-TPSR profiles of the Co_3O_4-B sample, and (d) CO_2 signal of the synthesized Co_3O_4 samples in the C_3H_8-TPSR process.

3.3. Catalytic performance

The propane conversion and CO_2 yield of the synthesized Co_3O_4 catalysts as functions of reaction temperature are shown in Fig. 7a and S3. The curves of CO_2 yield are close to the direct conversion of propane as the reaction temperature increases and no byproducts are detected by a mass spectrometer, which indicates that almost all propane has been completely converted to CO_2 and H_2O. To compare the catalytic activity more intuitively, the temperatures of 50% and 90% propane conversion (T_{50} and T_{90}) are summarized in Table 2. Obviously, the catalytic activities of the synthesized Co_3O_4 catalysts for propane oxidation decrease in the order Co_3O_4-B > Co_3O_4-F > Co_3O_4-E > Co_3O_4-S. The 90% propane conversion over Co_3O_4-B catalyst is achieved at 278 °C, lower than that of Co_3O_4-F (T_{90} = 285 °C), Co_3O_4-E (T_{90} = 295 °C), and Co_3O_4-S (T_{90} = 297 °C) catalysts. In addition, the propane consumption rate of Co_3O_4-B catalyst at 220 °C is 0.37 × 10^{-6} mol g^{-1} s^{-1}, which is higher than that of Co_3O_4-F (0.25 × 10^{-6} mol g^{-1} s^{-1}) and more than twice that of Co_3O_4-E and Co_3O_4-S (0.15 × 10^{-6} mol g^{-1} s^{-1}) catalysts. These results suggest that Co_3O_4-B exhibits the best catalytic performance for propane oxidation among all Co_3O_4 catalysts.

To further study the intrinsic activities of the catalysts, the specific reaction rates and turnover frequencies (TOFs) at specific temperatures are calculated. As listed in Table 2, the Co_3O_4-B sample shows the highest specific reaction rate (0.86 × 10^{-8} mol m^{-2} s^{-1}) and TOF (11.49 × 10^{-3} s^{-1}) at 220 °C, much higher than those over the Co_3O_4-E sample (0.42 × 10^{-8} mol m^{-2} s^{-1} and 6.09 × 10^{-3} s^{-1}), those over the Co_3O_4-F sample (0.70 × 10^{-8} mol m^{-2} s^{-1} and 9.01 × 10^{-3} s^{-1}), and those over the Co_3O_4-S sample (0.44 × 10^{-8} mol m^{-2} s^{-1} and 6.32 × 10^{-3} s^{-1}). Moreover, Fig. 7b and c directly show that Co_3O_4-B catalyst displays superior specific surface activity and a higher TOF for propane oxidation in terms of the temperature defined. From consideration of Co_3O_4-B, Co_3O_4-F, Co_3O_4-E, Co_3O_4-S samples with predominantly exposed {110}, {112}, {111}, and {110} facets, respectively, it can be inferred that a Co_3O_4 catalyst with a highly exposed {110} facet might exhibit the best catalytic oxidation activity, which is consistent with the previous reports that the {110} plane composed of abundant active Co^{3+} cations can offer sufficient active sites for the oxidation reaction [27,39]. Particularly, the lower specific catalytic activity of the Co_3O_4-S catalyst is probably due to its large crystallite size (29.5 nm) and weak reducibility. These results indicate that specific surface area, crystallite size, and highly exposed {110} facet, as well as low-temperature reducibility and reactive oxygen species, play a collective role in the catalytic performance of the Co_3O_4 catalysts for propane oxidation.

The apparent activation energy (E_a) of the synthesized Co_3O_4 catalysts is evaluated via the linear Arrhenius plot (Fig. 7d) and summarized in Table 2. The E_a value of Co_3O_4-B is 84.6 kJ mol^{-1}, while those of Co_3O_4-F, Co_3O_4-E, and Co_3O_4-S are 89.7, 96.7, and 99.4 kJ mol^{-1}, respectively. Generally, the catalytic activities obey an inverse trend to the E_a value. It is evident that the Co_3O_4-B catalyst exhibits the best catalytic activity for propane oxidation among all Co_3O_4 catalysts. Fig. 7e shows the effects of GHSV on the catalytic performance of the Co_3O_4-B catalyst for propane oxidation. It can be observed that the light-off temperature of propane conversion gradually rises with the GHSV increasing from 60,000 to 240,000 mL $g^{-1}h^{-1}$. Although the GHSV value increases to 240,000 mL $g^{-1}h^{-1}$, the T_{90} of Co_3O_4-B catalyst is only 288 °C. This result demonstrates that the GHSV has a visible impact on the propane conversion of the Co_3O_4-B catalyst, but the Co_3O_4-B catalyst

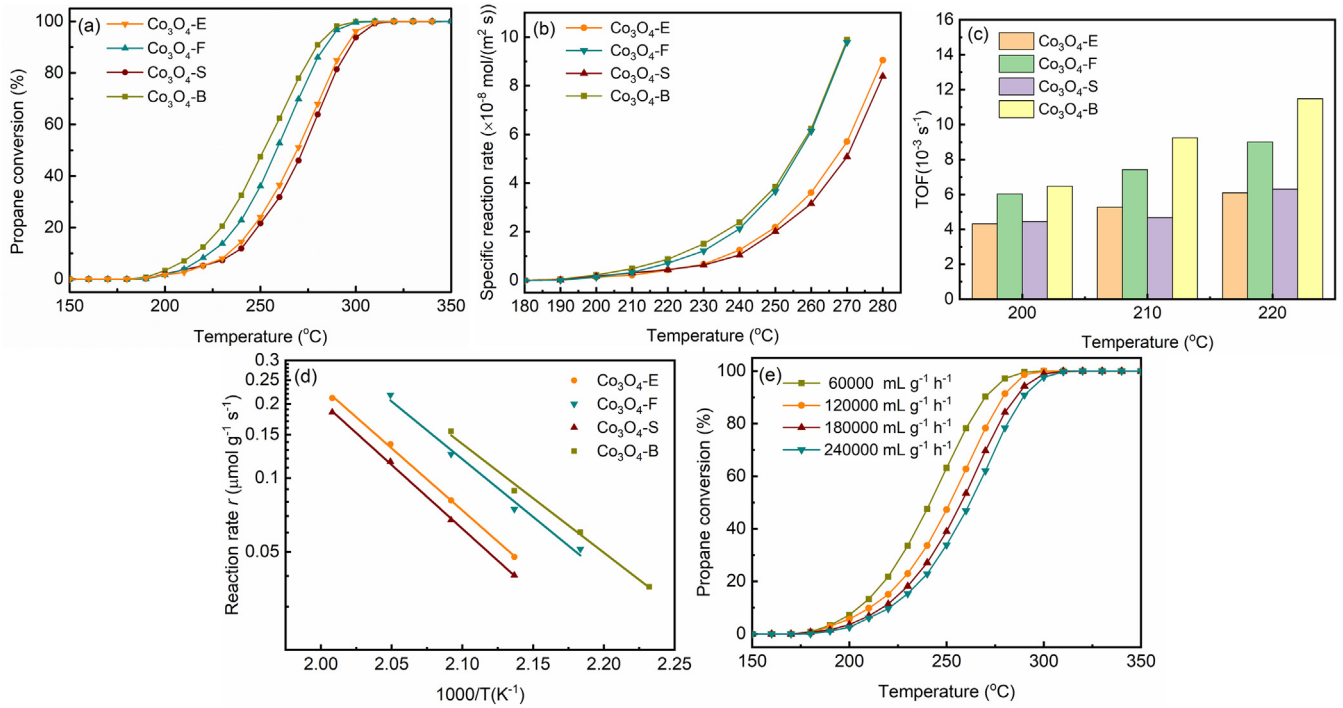

Fig. 7. (a) Propane conversion, (b) specific surface activity, (c) and TOFs for propane oxidation over the synthesized Co_3O_4 catalysts (reaction conditions: 100 mg catalyst, 0.2 vol% C_3H_8, 5 vol% O_2, and balance Ar, at a GHSV = 120,000 mL $g^{-1}h^{-1}$). (d) The corresponding Arrhenius plots; a conversion level < 15% was employed to make Arrhenius plots and to calculate apparent activation energies. (e) The influence of GHSV on the catalytic activity of Co_3O_4-B catalyst for propane oxidation. (Reaction conditions: 100 mg catalyst, 0.2 vol% C_3H_8, 5 vol% O_2, and balance Ar. Total gas flow rates: 100–400 mL min^{-1}.)

Table 2
T_{50} and T_{90} values, reaction rates, turnover frequencies (TOFs), and apparent activation energies (E_a) for propane oxidation over the synthesized Co_3O_4 catalysts.

Catalyst	T_{50} (°C)	T_{50} (H) (°C) [a]	T_{90} (°C)	T_{90} (H) (°C) [a]	Reaction rate (10^{-6} mol g^{-1} s^{-1})[b]	Reaction rate (10^{-8} mol m^{-2} s^{-1})[b]	O_2 uptake (μmol g^{-1})[c]	TOFs (10^{-3} s^{-1})[b]	E_a (kJ mol^{-1})
Co_3O_4-E	269	289	295	312	0.15	0.42	14.09	6.09	96.7
Co_3O_4-F	258	281	285	307	0.25	0.70	15.18	9.01	89.7
Co_3O_4-S	272	295	297	319	0.15	0.44	12.10	6.32	99.4
Co_3O_4-B	250	269	278	300	0.37	0.86	16.06	11.49	84.6

[a] Humid reaction conditions: 0.2 vol% C_3H_8, 5 vol% O_2, 2.5 vol% H_2O, Ar balance, GHSV = 120,000 mL $g^{-1}h^{-1}$.
[b] Reaction rates and turnover frequencies (TOFs) calculated at low conversion in a kinetically controlled regime at 220 °C for propane oxidation.
[c] Oxygen uptakes of Co_3O_4 samples were obtained at 220 °C.

Table 3
Comparison of the catalytic results for Co_3O_4-B catalyst with those reported in the literature.

Catalyst	Reaction conditions	GHSV (mL $g^{-1}h^{-1}$)	T_{50} (°C)	T_{90} (°C)	Ref.
Pt-$LaCoO_3$	0.8% C_3H_8, 99.2% Air	150,000	325	460	[45]
$CoCeO_x$-70	0.2% C_3H_8, 5% O_2, 97.8% Ar	120,000	265	310	[46]
Pt-10Nb/Al_2O_3	0.2% C_3H_8, 5% O_2, 97.8% N_2	80,000	210	270	[47]
$Ni_{0.27}Co_{2.73}O_4$	1% C_3H_8, 10% O_2, 9%N_2, 80% Ar	60,000	320	390	[42]
Mn-Fe/CeO_2-P1	0.8% C_3H_8, 20% O_2, 79.2% N_2	60,000	318	382	[48]
Co_3O_4	0.3% C_3H_8, 10% O_2, 89.7% N_2	60,000	300	330	[49]
γ-MnO_x	0.2% C_3H_8, 5% O_2, 94.8% Ar	60,000	270	310	[43]
LM-EG	0.2% C_3H_8, 99.8% Air	30,000	275	310	[50]
$NiCeO_x$-4	0.2% C_3H_8, 2% O_2, 97.8% Ar	30,000	275	300	[41]
Co_3O_4/ZSM-5	0.2% C_3H_8, 2% O_2, 97.8% N_2	30,000	235	260	[51]
Pd/ZSM	0.2% C_3H_8, 2% O_2, 97.8% N_2	30,000	326	332	[51]
NiO-Co(0.3)	0.1% C_3H_8, 18% O_2, 81.9% N_2	30,000	194	236	[20]
MnCu24	2% C_3H_8, 20% O_2, 78% He	20,000	280	320	[44]
Co_3O_4-B	0.2% C_3H_8, 5% O_2, 97.8% Ar	120,000	250	278	This work
Co_3O_4-B	0.2% C_3H_8, 5% O_2, 97.8% Ar	60,000	242	268	This work

could retain good catalytic performance at a high GHSV. Additionally, Table 3 lists the catalytic activities of typical catalysts reported in the literature for propane oxidation. Obviously, Co_3O_4-B catalyst (T_{90} = 278 °C) exhibits better catalytic performance for propane

oxidation than those in previous literature, such as $NiCeO_x$-4 (T_{90} = 300 °C) [41], $Ni_{0.27}Co_{2.73}O_4$ (T_{90} = 390 °C) [42], Pd/ZSM (T_{90} = 332 °C), γ-MnO_x (T_{90} = 310 °C) [43], and MnCu24 (T_{90} = 320 °C) [44]. This indicates that the Co_3O_4-B catalyst, as a substitute for traditional noble metal catalysts, has great potential in the removal of alkane VOC owing to its good catalytic activity and low cost.

3.4. Water vapor resistance

In practical applications, water vapor is usually present in the feed gas or generated along with the propane oxidation reaction, which can be competitively adsorbed and occupy the active sites of the catalysts. To explore the effect of water vapor, 2.5 vol% H_2O is added into the feed gas. As shown in Fig. 8a, the curves of propane conversion shift significantly to a higher temperature than that under dry conditions, indicating that the existence of water vapor in feed gas has a negative effect on the catalytic activities of all Co_3O_4 catalysts. For example, the T_{50}/T_{90} values of Co_3O_4-B catalyst are obtained at 250 °C/278 °C under dry conditions, while they increase to 269 °C/300 °C under humid conditions. Nevertheless, Co_3O_4-B still shows the highest catalytic performance among all Co_3O_4 catalysts under humid conditions. To deeply reveal the influence of water vapor on catalyst activity, the specific reaction rates of propane oxidation over Co_3O_4 samples in humid condition were calculated and are shown in Fig. 8b. Specifically, to achieve the same specific reaction rate (2×10^{-8} mol m^{-2} s^{-1}), the reaction temperature of the Co_3O_4-B catalyst under humid conditions needs to increase by 14 °C compared with dry conditions (Fig. 8c), which is lower than for Co_3O_4-F (19 °C), Co_3O_4-E (20 °C), and Co_3O_4-S (22 °C) catalysts. This demonstrates that the Co_3O_4-B catalyst shows the best resistance to water vapor among all synthesized Co_3O_4 catalysts. In addition, the C_3H_8-TPSR-H experiment in water vapor is carried out to further understand the influence of water vapor. As shown in Fig. 8d and e, the C_3H_8-TPSR-H process of the Co_3O_4-B catalyst is similar to the C_3H_8-TPSR process, except for a smaller amount of CO_2 production and a higher peak temperature (increasing from 205 to 225 °C). This indicates that the existence of water vapor in feed gas inhibits the adsorption and activation of propane on the catalyst surface, and thus reduces the catalyst activity. From the CO_2 signal of all Co_3O_4 samples (Fig. 8f), Co_3O_4-B has the largest amount of CO_2 production and lowest peak temperature in the C_3H_8-TPSR-H process. Therefore, it is reasonable to conclude that Co_3O_4-B shows the highest catalytic activity and better water-resistance performance for propane oxidation under humid conditions, and the decline of catalytic activity under humid conditions is due to the existence of water vapor, which inhibits the adsorption and activation of propane on the surface.

3.5. Stability

The long-term stability and recycle stability have a substantial influence on practical application of catalysts. As shown in Fig. 9a, the catalytic activity of the Co_3O_4-B catalyst visibly declines with the introduction of 2.5 vol% H_2O into the reaction stream at 280 °C, but no significant decline can be observed after reaction for 40 h, which indicates excellent long-term stability of the Co_3O_4-B catalyst during propane oxidation under humid conditions. In addition, the propane conversion can return to the original values once water vapor is cut off, demonstrating that this deactivation is reversible. This reversible deactivation can be explained by C_3H_8-TPSR-H results that water vapor occupies the active sites of the catalyst, and then inhibits the adsorption and activation of propane on the surface. Besides the long-term stability test, a cycle stability test of the Co_3O_4-B catalyst under humid conditions is carried out and shown in Fig. 9b. No significant change in catalytic activity of the Co_3O_4-B catalyst is observed after four recycle experiments, the T_{50} values are 269, 268, 269, and 268 °C for the first,

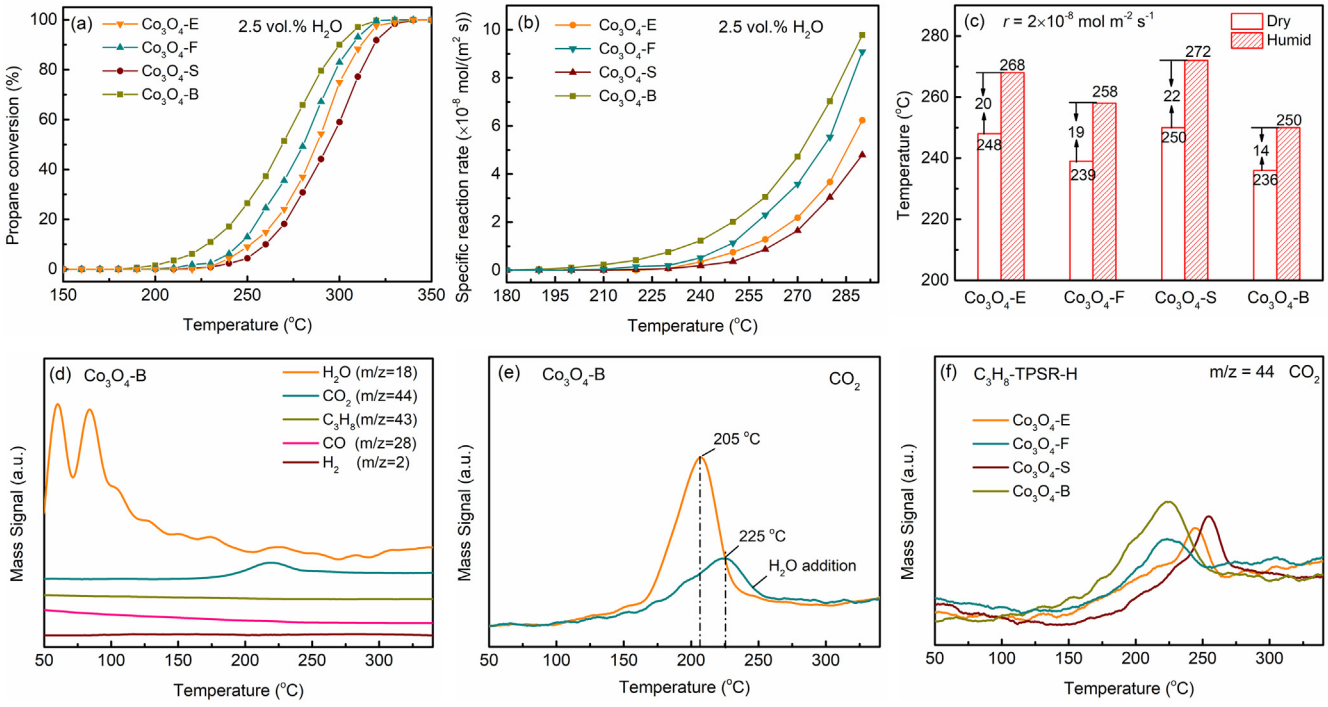

Fig. 8. (a) Propane conversion. (b) Specific surface activity of propane oxidation over the synthesized Co_3O_4 catalysts under humid conditions (reaction conditions: 100 mg catalyst, 0.2 vol% C_3H_8, 5 vol% O_2, 2.5 vol% H_2O, and balance Ar, at GHSV = 120,000 mL $g^{-1}h^{-1}$). (c) Comparison of reaction temperatures of the synthesized Co_3O_4 catalysts at the specific reaction rate of 2×10^{-8} mol m^{-2} s^{-1} under dry and humid conditions. (d) C_3H_8-TPSR-H profiles of the Co_3O_4-B sample (under humid conditions). (e) Comparison of CO_2 signal for Co_3O_4-B sample during C_3H_8-TPSR process under dry and humid conditions. (f) CO_2 signal of the synthesized Co_3O_4 samples during the C_3H_8-TPSR-H process.

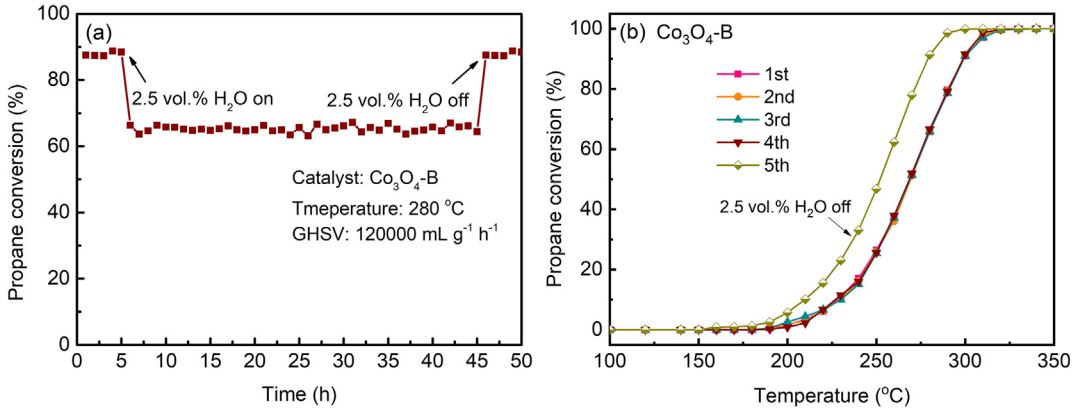

Fig. 9. (a) The long-term stability and (b) the recycle stability of Co_3O_4-B catalyst for propane oxidation under humid conditions. (Reaction conditions: 100 mg catalyst, 0.2 vol% C_3H_8, 5 vol% O_2, 2.5 vol% H_2O, and balanced Ar, at GHSV = 120,000 mL $g^{-1}h^{-1}$.)

second, third, and fourth cycle, respectively, and T_{90} is 300 °C for all cycles. When the 2.5 vol% H_2O is removed from the reactant gas, the propane conversion can almost be restored to the original values, where the T_{50} and T_{90} are 250 and 280 °C, respectively. The XRD and SEM patterns of the spent Co_3O_4-B catalyst after the long-term stability test were also investigated. As shown in Fig. S4, the XRD patterns and morphology of the spent Co_3O_4-B catalyst did not change significantly compared with those of fresh Co_3O_4-B, suggesting the excellent structural stability of the Co_3O_4-B catalyst. These results indicate that the Co_3O_4-B catalyst has satisfactory recycle and long-term stability even under humid conditions.

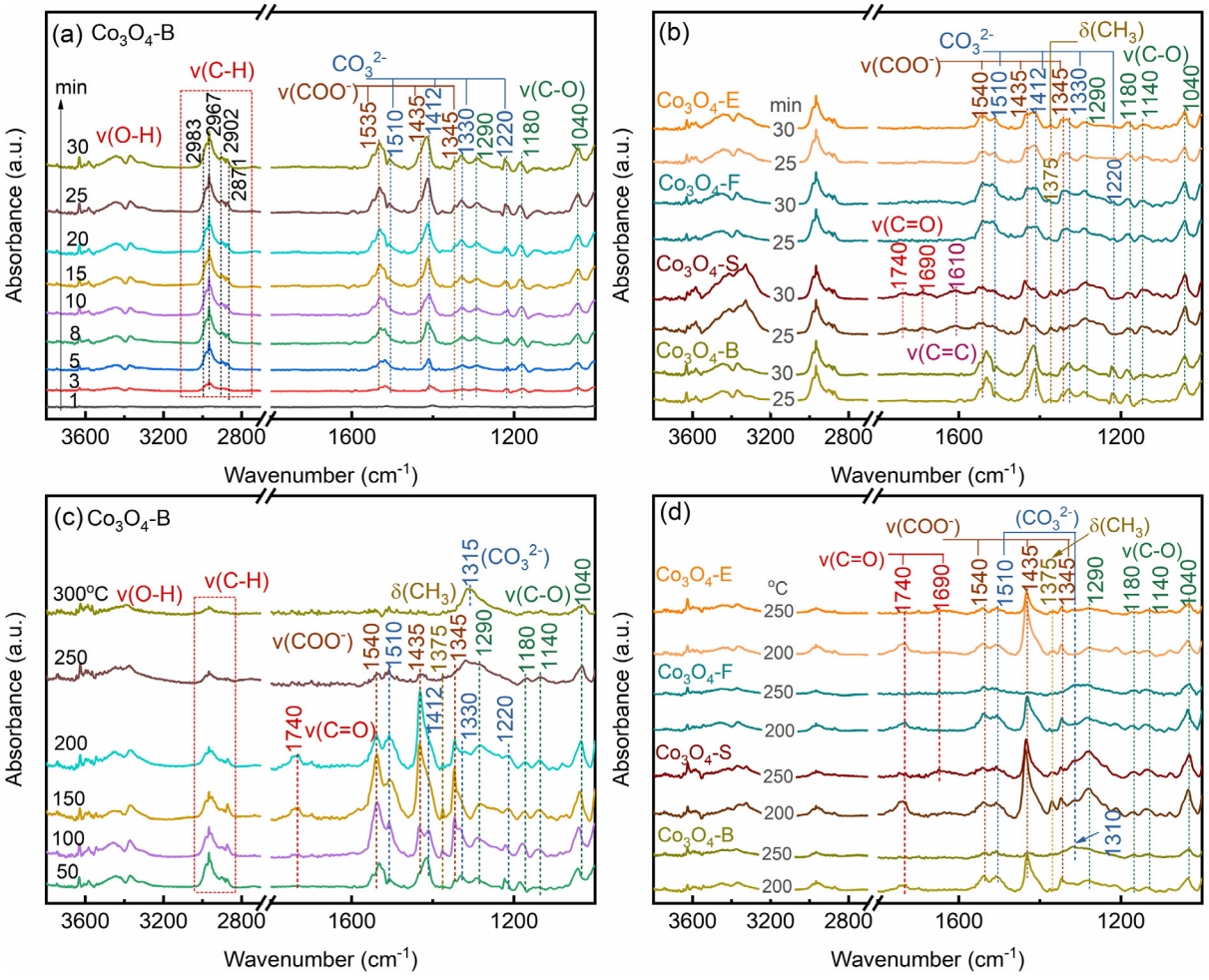

Fig. 10. (a) In situ DRIFT spectra of C_3H_8 adsorption (0.2 vol% C_3H_8/Ar) over Co_3O_4-B sample at 50 °C. (b) Comparison of in situ DRIFT spectra over the synthesized Co_3O_4 samples after C_3H_8 adsorption of 25 and 30 min. (c) In situ DRIFT spectra of C_3H_8 oxidation (0.2 vol% C_3H_8, 5 vol% O_2/Ar) over Co_3O_4-B sample at 50–300 °C. (d) Comparison of in situ DRIFTS spectra over the synthesized Co_3O_4 samples after C_3H_8 oxidation at 200 and 250 °C.

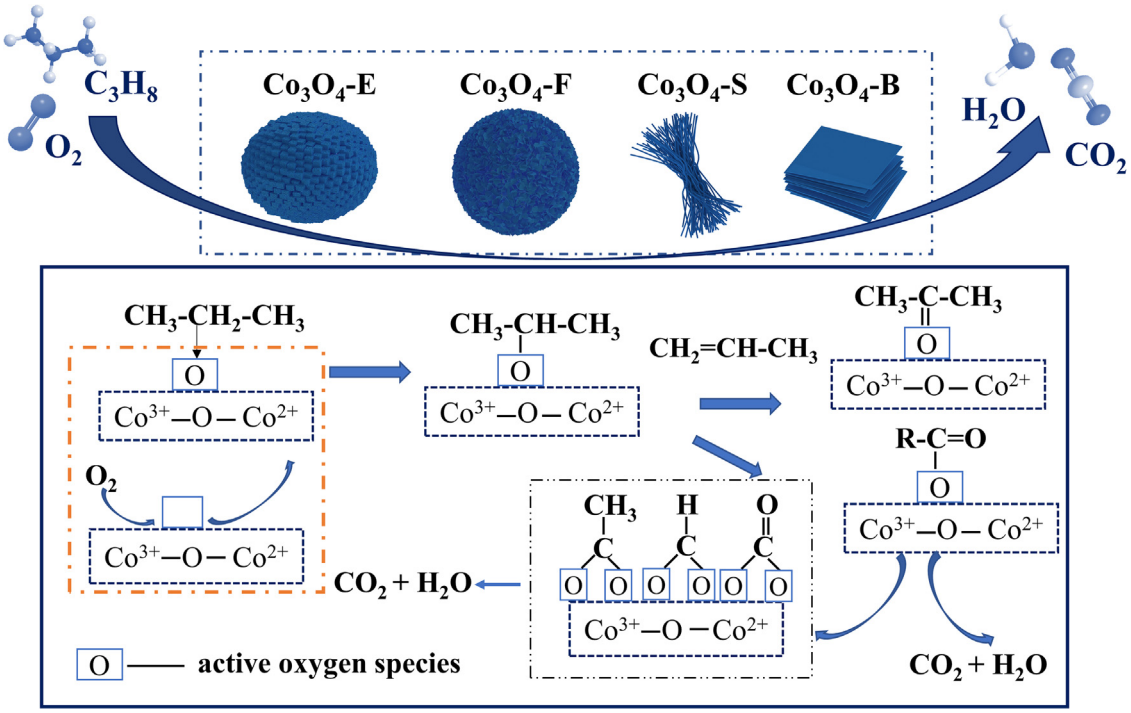

Scheme 1. Proposed reaction mechanism of propane oxidation on Co_3O_4 catalysts.

3.6. In situ diffuse reflectance infrared Fourier transform spectroscopy of propane adsorption and oxidation

In situ DRIFTS measurements were conducted to track the intermediates in the propane adsorption and oxidation process over the synthesized Co_3O_4 samples and to study the reaction mechanism. Fig. 10a displays in situ DRIFT spectra of propane adsorption on a Co_3O_4-B sample at 50 °C. The strong absorption peaks detected at 2840–3050 cm^{-1} are ascribed to the asymmetric CH_3 and CH_2 stretching vibrations of adsorbed propane [47,52,53]. Broad peaks around 3372 and 3442 cm^{-1} are assigned to the ν(O-H) band of the hydroxyl group or adsorbed water [54,55]. In addition, multiple absorption bands at 1000–1800 cm^{-1} attributed to the carboxylate and carbonate species develop significantly and reach a stable level with time on stream. Briefly, the peaks at 1540, 1435, and 1345 cm^{-1} correspond to the symmetrical stretching vibration of acetate/formate species, while the bands at 1510, 1415, and 1377 and 1280 cm^{-1} are assigned to the bidentate/uncoordinated CO_3^{2-}, δ(CH_3), and ν(C—O) species, respectively [56–59]. Other peaks between 1000 and 1200 cm^{-1} ascribed to the C—O bands (1180, 1040 cm^{-1}) of alkoxide species are also detected during the propane adsorption process [54,60]. This indicates that C_3H_8 can be partially oxidatively cracked and reacts with the labile oxygen in the catalyst to a certain extent. The adsorption process of Co_3O_4-E and Co_3O_4-F is similar to that of Co_3O_4-B, except for the Co_3O_4-S sample (as shown in Fig. 10b and S5), where additional bands at 1690, 1740, and 1613 cm^{-1} assigned to the ν_{as} (C=O) stretching vibrations of acetone and carbonyl group with an aliphatic ester group and the ν(C=C) stretching vibration are observed on the surface [59,61–63]. This difference may be closely related to their surface properties, such as active oxygen species and redox properties.

Subsequently, the feed gas was switched to 0.2 vol% C_3H_8, 5 vol % O_2, and 94.8 vol% Ar, and in situ DRIFT spectra of each Co_3O_4 sample were recorded after 25 min of reaction at the specific temperatures (50, 100, 150, 200, 250, and 300 °C). As the reaction progresses over the Co_3O_4-B sample (Fig. 10c), the peak intensities of the C—H stretching vibrations of propane in the range of 2840–3050 cm^{-1} gradually decrease, while the multiple peaks at 1540 cm^{-1} (ν_{as} COO^-), 1435 cm^{-1} (ν_s COO^-), 1345 cm^{-1} (ν_s COO^-), and 1510 cm^{-1} (CO_3^{2-}) assigned to formate/acetate species and carbonate species first continuously increase and then decrease with temperature on stream. Meanwhile, the peak of the C=O stretching species (1740 cm^{-1}) also first gradually increases and then decreases throughout the reaction, and new bands assigned to bidentate carbonate species (1315 cm^{-1}) are detected at higher temperature [61,64]. The result implies that a series of intermediates (carboxylate/carbonate species) are involved in the propane oxidation reaction, which could be oxidized further by oxygen into final products of CO_2 and H_2O. The DRIFT spectra of C_3H_8 oxidation over Co_3O_4-E, Co_3O_4-F, and Co_3O_4-S samples are shown in Fig. S5, and their DRIFT spectra of propane oxidation at 200 and 250 °C are shown in Fig. 10d. Notably, the evolution of the surface intermediates on Co_3O_4 catalysts varies with the morphologies, where more intermediates (ν(C=O), 1690 cm^{-1}) accumulate on the Co_3O_4-S and Co_3O_4-E surfaces, which will occupy the active sites and then affect the catalyst activity.

Even though the evolution of surface species is a bit different, the kind of intermediates on the Co_3O_4 surface is similar. Therefore, a possible reaction pathway of propane oxidation on Co_3O_4 catalysts is proposed (as shown in Scheme 1). First, the gaseous C_3H_8 adsorbed at the active sites of the Co_3O_4 catalysts to form chemisorbed C_3H_{8-n}. Then, the activated C_3H_{8-n} species reacted with the reactive oxygen species, leading to the cracking of first C—C bonds or additional C—H bonds to form intermediates, such as carboxylate (acetate/formate) and carbonate species. Simultaneously, some intermediates such as aliphatic ester group and acetone also accumulated on the catalyst surface, which would react further with the oxygen species to form the carboxylate or carbonate species. Finally, these adsorbed intermediates could be oxidized further into CO_2 and H_2O. Meanwhile, gas-phase O_2 would be adsorbed on the surface and be activated to reactive oxygen species.

4. Conclusions

In summary, hierarchically structured Co_3O_4 materials with different morphologies (ellipsoidal, flowerlike, book-shaped, spindle-like) were controllably synthesized via hydrothermal methods, and their catalytic properties greatly depended on their morphology. Among these catalysts, book-shaped Co_3O_4-B catalyst exhibits the best catalytic performance for propane oxidation, for which T_{50} and T_{90} are 250 and 278 °C, respectively (GHSV = 120,000 mL g^{-1}h^{-1}). Simultaneously, Co_3O_4-B catalyst shows the highest propane oxidation rate (0.86×10^{-8} mol m^{-2} s^{-1}) and the highest turnover frequency (TOF = 11.49×10^{-3} s^{-1}) at 220 °C. It has been demonstrated that the book-shaped structure (Co_3O_4-B) provides a larger specific surface area, a smaller crystal size, and a highly exposed {1 1 0} facet, which make the catalyst exhibit favorable low-temperature reducibility and oxygen mobility, and thus promote the adsorption and activation of propane on the catalyst surface. In addition, a possible reaction pathway of propane oxidation over Co_3O_4 has been proposed: C_3H_8 is adsorbed and activated on the Co_3O_4 surface and then transformed into C_3H_{8-n} species, which will bond with activated oxygen species to form carbon–oxygen intermediates, and then be completely oxidized into CO_2 and H_2O. C_3H_8-TPSR-H studies indicate that there is competitive adsorption between propane and water vapor, which leads to a decline of propane conversion. However, Co_3O_4-B catalyst shows great resistance to water vapor, and could retain excellent stability and reusability in practical propane oxidation (2.5 vol% H_2O). This study provides a morphology control strategy for designing highly efficient catalysts for VOC removal.

Declaration of Competing Interest

The authors declare that they have no known competing financial interests or personal relationships that could have appeared to influence the work reported in this paper.

Acknowledgment

We gratefully acknowledge the financial support provided by the National Key Research and Development Program of China (2016YFB0600305).

Appendix A. Supplementary material

Supplementary data to this article can be found online at https://doi.org/10.1016/j.jcat.2021.02.014.

References

[1] G.R. Parmar, N.N. Rao, Emerging control technologies for volatile organic compounds, Crit. Rev. Environ. Sci. Technol. 39 (2008) 41–78.
[2] J. Pei, J.S. Zhang, On the performance and mechanisms of formaldehyde removal by chemi-sorbents, Chem. Eng. J. 167 (2011) 59–66.
[3] Q. Yuan, Z. Wu, Y. Jin, F. Xiong, W. Huang, Surface chemistry of formaldehyde on rutile TiO_2 (110) surface: photocatalysis vs thermal-catalysis, J. Phys. Chem. C 118 (2014) 20420–20428.
[4] X. Zhu, S. Zhang, Y. Yang, C. Zheng, J. Zhou, X. Gao, X. Tu, Enhanced performance for plasma-catalytic oxidation of ethyl acetate over $La_{1-x}Ce_xCoO_{3+\delta}$ catalysts, Appl. Catal. B 213 (2017) 97–105.
[5] W. Si, Y. Wang, S. Zhao, F. Hu, J. Li, A facile method for in situ preparation of the MnO_2/$LaMnO_3$ catalyst for the removal of toluene, Environ. Sci. Technol. 50 (2016) 4572–4578.
[6] H. Huang, Y. Xu, Q. Feng, D.Y.C. Leung, Low temperature catalytic oxidation of volatile organic compounds: a review, Catal. Sci. Technol. 5 (2015) 2649–2669.
[7] H. Yang, C. Ma, G. Wang, Y. Sun, J. Cheng, Z. Zhang, X. Zhang, Z. Hao, Fluorine-enhanced Pt/ZSM-5 catalysts for low-temperature oxidation of ethylene, Catal. Sci. Technol. 7 (2018) 1988–1996.
[8] R. Peng, X. Sun, S. Li, L. Chen, M. Fu, J. Wu, D. Ye, Shape effect of Pt/CeO_2 catalysts on the catalytic oxidation of toluene, Chem. Eng. J. 306 (2016) 1234–1246.
[9] E. Hong, C. Kim, D.-H. Lim, H.-J. Cho, C.-H. Shin, Catalytic methane combustion over Pd/ZrO_2 catalysts: Effects of crystalline structure and textural properties, Appl. Catal. B 232 (2018) 544–552.
[10] H. Tan, J. Wang, S. Yu, K. Zhou, Support morphology-dependent catalytic activity of Pd/CeO_2 for formaldehyde oxidation, Environ. Sci. Technol. 49 (2015) 8675–8682.
[11] J. Chen, D. Yan, Z. Xu, X. Chen, X. Chen, W. Xu, H. Jia, J. Chen, A Novel redox precipitation to synthesize Au-doped α-MnO_2 with high dispersion toward low-temperature oxidation of formaldehyde, Environ. Sci. Technol. 52 (2018) 4728–4737.
[12] S. Mo, S. Li, J. Li, Y. Deng, S. Peng, J. Chen, Y. Chen, Rich surface Co(iii) ions-enhanced Co nanocatalyst benzene/toluene oxidation performance derived from Co(II)Co(III) layered double hydroxide, Nanoscale 8 (2016) 15763–15773.
[13] D.K. Pappas, T. Boningari, P. Boolchand, P.G. Smirniotis, Novel manganese oxide confined interweaved titania nanotubes for the low-temperature Selective Catalytic Reduction (SCR) of NO_x by NH_3, J. Catal. 334 (2016) 1–13.
[14] X. Wang, W. Zhao, T. Zhang, Y. Zhang, L. Jiang, S. Yin, Facile fabrication of shape-controlled $Co_xMn_yO_\beta$ nanocatalysts for benzene oxidation at low temperatures, Chem. Commun. 54 (2018) 2154–2157.
[15] H. Arandiyan, Y. Wang, H. Sun, M. Rezaei, H. Dai, Ordered meso- and macroporous perovskite oxide catalysts for emerging applications, Chem. Commun. 54 (2018) 6484–6502.
[16] Z. Wu, M. Li, S.H. Overbury, On the structure dependence of CO oxidation over CeO_2 nanocrystals with well-defined surface planes, J. Catal. 285 (2012) 61–73.
[17] C. Ma, D. Wang, W. Xue, B. Dou, H. Wang, Z. Hao, Investigation of formaldehyde oxidation over Co_3O_4-CeO_2 and Au/Co_3O_4-CeO_2 catalysts at room temperature: effective removal and determination of reaction mechanism, Environ. Sci. Technol. 45 (2011) 3628–3634.
[18] T.M. Nyathi, N. Fischer, A.P.E. York, D.J. Morgan, G.J. Hutchings, E.K. Gibson, P.P. Wells, C.R.A. Catlow, M. Claeys, Impact of nanoparticle-support interactions in Co_3O_4/Al_2O_3 catalysts for the preferential oxidation of carbon monoxide, ACS Catal. 9 (2019) 7166–7178.
[19] Y. Liu, H. Dai, J. Deng, S. Xie, H. Yang, W. Tan, W. Han, Y. Jiang, G. Guo, Mesoporous Co_3O_4-supported gold nanocatalysts: Highly active for the oxidation of carbon monoxide, benzene, toluene, and o-xylene, J. Catal. 309 (2014) 408–418.
[20] T. Cai, J. Yuan, L. Zhang, L. Yang, Q. Tong, M. Ge, B. Xiao, X. Zhang, K. Zhao, D. He, Ni–Co–O solid solution dispersed nanocrystalline Co_3O_4 as a highly active catalyst for low-temperature propane combustion, Catal. Sci. Technol. 8 (2018) 5416–5427.
[21] J. Bae, D. Shin, H. Jeong, B.-S. Kim, J.W. Han, H. Lee, Highly water-resistant La-doped Co_3O_4 catalyst for CO oxidation, ACS Catal. 9 (2019) 10093–10100.
[22] Q. Ren, Z. Feng, S. Mo, C. Huang, S. Li, W. Zhang, L. Chen, M. Fu, J. Wu, D. Ye, 1D-Co3O4, 2D-Co3O4, 3D-Co3O4 for catalytic oxidation of toluene, Catal. Today 332 (2019) 160–167.
[23] X. Zhou, Z. Liu, Y. Wang, Y. Ding, Facet effect of Co_3O_4 nanocrystals on visible-light driven water oxidation, Appl. Catal. B 237 (2018) 74–84.
[24] Y. Sun, J. Liu, J. Song, S. Huang, N. Yang, J. Zhang, Y. Sun, Y. Zhu, Exploring the effect of Co_3O_4 nanocatalysts with different dimensional architectures on methane combustion, ChemCatChem 8 (2016) 540–545.
[25] B. Bai, H. Arandiyan, J. Li, Comparison of the performance for oxidation of formaldehyde on nano-Co_3O_4, 2D-Co_3O_4, and 3D-Co_3O_4 catalysts, Appl. Catal. B 142–143 (2013) 677–683.
[26] L. Hu, Q. Peng, Y. Li, Selective synthesis of Co_3O_4 nanocrystal with different shape and crystal plane effect on catalytic property for methane combustion, J. Am. Chem. Soc. 130 (2008) 16136–16137.
[27] X. Xie, Y. Li, Z.Q. Liu, M. Haruta, W. Shen, Low-temperature oxidation of CO catalysed by Co_3O_4 nanorods, Nature 458 (2009) 746–749.
[28] Q. Ren, S. Mo, R. Peng, Z. Feng, M. Zhang, L. Chen, M. Fu, J. Wu, D. Ye, Controllable synthesis of 3D hierarchical Co_3O_4 nanocatalysts with various morphologies for the catalytic oxidation of toluene, J. Mater. Chem. A 6 (2018) 498–509.
[29] Y. Qin, H. Wang, C. Dong, Z. Qu, Evolution and enhancement of the oxygen cycle in the catalytic performance of total toluene oxidation over manganese-based catalysts, J. Catal. 380 (2019) 21–31.
[30] C. Reed, Y.-K. Lee, S.T. Oyama, Structure and oxidation state of silica-supported manganese oxide catalysts and reactivity for acetone oxidation with ozone, J. Phys. Chem. B 110 (2006) 4207–4216.
[31] A.N. Desikan, L. Huang, S.T. Oyama, Oxygen chemisorption and laser Raman spectroscopy of unsupported and sillica-supported molybdenum oxide, J. Phys. Chem. 95 (1991) 10050–10056.
[32] M.D. Farahani, M. Wolf, T.O.P. Mkhwanazi, M. Claeys, H.B. Friedrich, Operando experimental evidence on the central role of oxygen vacancies during methane combustion, J. Catal. 390 (2020) 184–195.
[33] S.T. Oyama, X. Zhang, J. Lu, Y. Gu, T. Fujitani, Epoxidation of propylene with H_2 and O_2 in the explosive regime in a packed-bed catalytic membrane reactor, J. Catal. 257 (2008) 1–4.
[34] J. Mu, L. Zhang, G. Zhao, Y. Wang, The crystal plane effect on the peroxidase-like catalytic properties of Co_3O_4 nanomaterials, Phys. Chem. Chem. Phys. 16 (2014) 15709–15716.
[35] M. Li, F. Bi, Y. Xu, P. Hao, K. Xiang, Y. Zhang, S. Chen, J. Guo, X. Guo, W. Ding, Effect of residual chlorine on the catalytic performance of Co_3O_4 for CO oxidation, ACS Catal. 9 (2019) 11676–11684.
[36] C. Dong, Z. Qu, Y. Qin, Q. Fu, H. Sun, X. Duan, Revealing the highly catalytic performance of spinel $CoMn_2O_4$ for toluene oxidation: involvement and

replenishment of oxygen species using in situ designed-TP techniques, ACS Catal. (2019) 6698–6710.
[37] W. Liu, R. Liu, H. Zhang, Q. Jin, Z. Song, X. Zhang, Fabrication of Co_3O_4 nanospheres and their catalytic performances for toluene oxidation: The distinct effects of morphology and oxygen species, Appl. Catal. A 597 (2020) 117539.
[38] Y. Cai, J. Xu, Y. Guo, J. Liu, Ultrathin, polycrystalline, two-dimensional Co_3O_4 for low-temperature CO oxidation, ACS Catal. 9 (2019) 2558–2567.
[39] K. Wang, Y. Cao, J. Hu, Y. Li, J. Xie, D. Jia, Solvent-free chemical approach to synthesize various morphological Co_3O_4 for CO oxidation, ACS Appl. Mater. Interfaces 9 (2017) 16128–16137.
[40] S. Mo, Q. Zhang, Y. Sun, M. Zhang, J. Li, Q. Ren, M. Fu, J. Wu, L. Chen, D. Ye, Gaseous CO and toluene co-oxidation over monolithic core-shell Co_3O_4-based hetero-structured catalysts, J. Mater. Chem. A 27 (2019) 16197–16210.
[41] Z. Hu, S. Qiu, Y. You, Y. Guo, Y. Guo, L. Wang, W. Zhan, G. Lu, Hydrothermal synthesis of $NiCeO_x$ nanosheets and its application to the total oxidation of propane, Appl. Catal. B 225 (2017) 110–120.
[42] Z. Ren, Z. Wu, W. Song, W. Xiao, Y. Guo, J. Ding, S.L. Suib, P.-X. Gao, Low temperature propane oxidation over Co_3O_4 based nano-array catalysts: Ni dopant effect, reaction mechanism and structural stability, Appl. Catal. B 180 (2016) 150–160.
[43] Y. Xie, Y. Yu, X. Gong, Y. Guo, Y. Guo, Y. Wang, G. Lu, Effect of the crystal plane figure on the catalytic performance of MnO_2 for the total oxidation of propane, CrystEngComm 17 (2015) 3005–3014.
[44] M. Morales, B. Barbero, L. Cadus, Total oxidation of ethanol and propane over Mn-Cu mixed oxide catalysts, Appl. Catal. B 67 (2006) 229–236.
[45] Y. Luo, J. Zuo, X. Feng, Q. Qian, Y. Zheng, D. Lin, B. Huang, Q. Chen, Good interaction between well dispersed Pt and $LaCoO_3$ nanorods achieved rapid Co^{3+}/Co^{2+} redox cycle for total propane oxidation, Chem. Eng. J. 357 (2019) 395–403.
[46] W. Zhu, X. Chen, J. Jin, X. Di, C. Liang, Z. Liu, Insight into catalytic properties of Co_3O_4-CeO_2 binary oxides for propane total oxidation, Chin. J. Catal. 41 (2020) 679–690.
[47] Z. Wang, Z. Huang, J.T. Brosnahan, S. Zhang, Y. Guo, Y. Guo, L. Wang, Y. Wang, W. Zhan, Ru/CeO_2 catalyst with optimized CeO_2 support morphology and surface facets for propane combustion, Environ. Sci. Technol. 53 (2019) 5349–5358.
[48] Y. Xiao, W. Zhao, K. Zhang, Y. Zhang, X. Wang, T. Zhang, X. Wu, C. Chen, L. Jiang, Facile synthesis of Mn-Fe/CeO_2 nanotubes by gradient electrospinning and their excellent catalytic performance for propane and methane oxidation, Dalton Trans. 46 (2017) 16967–16972.
[49] W. Tang, W. Xiao, S. Wang, Z. Ren, J. Ding, P.-X. Gao, Boosting catalytic propane oxidation over PGM-free Co_3O_4 nanocrystal aggregates through chemical leaching: A comparative study with Pt and Pd based catalysts, Appl. Catal. B 226 (2018) 585–595.
[50] N. Miniajluk, J. Trawczyński, M. Zawadzki, Properties and catalytic performance for propane combustion of $LaMnO_3$ prepared under microwave-assisted glycothermal conditions: Effect of solvent diols, Appl. Catal. A 531 (2017) 119–128.
[51] Z. Zhu, G. Lu, Z. Zhang, Y. Guo, Y. Guo, Y. Wang, A high active and stable Co_3O_4/ZSM-5 catalyst for propane oxidation: An effect of preparation method, ACS Catal. 3 (2013) 1154–1164.
[52] W. Tang, J. Weng, X. Lu, L. Wen, A. Suburamanian, C.-Y. Nam, P.-X. Gao, Alkali-metal poisoning effect of total CO and propane oxidation over Co_3O_4 nanocatalysts, Appl. Catal. B 256 (2019) 117859.
[53] Y. Xie, Y. Guo, Y. Guo, L. Wang, W. Zhan, Y. Wang, X.-Q. Gong, G. Lu, A highly-efficient La–MnO_x catalyst for propane combustion: the promotional role of La and the effect of the preparation method, Catal. Sci. Technol. 6 (2016) 8222–8233.
[54] W. Yang, Y. Peng, Y. Wang, Y. Wang, H. Liu, Z.A. Su, W. Yang, J. Chen, W. Si, J. Li, Controllable redox-induced in-situ growth of MnO_2 over Mn_2O_3 for toluene oxidation: active heterostructure interfaces, Appl. Catal. B 278 (2020) 119279.
[55] X. Sun, J. Lin, Y. Wang, L. Li, X. Pan, Y. Su, X. Wang, Catalytically active Ir^0 species supported on Al_2O_3 for complete oxidation of formaldehyde at ambient temperature, Appl. Catal. B 268 (2020) 118741.
[56] Y. Fang, L. Li, J. Yang, S. Hoang, L. Wang, J. Xu, W. Yang, C. Pan, Y. Zhu, H. Deng, Z. Luo, C. Sun, D. Gao, Z. Li, Y. Guo, Engineering the nucleophilic active oxygen species in $CuTiO_x$ for efficient low-temperature propene combustion, Environ. Sci. Technol. 54 (2020) 15476–15488.
[57] T. Zhang, X. Lang, A. Dong, X. Wan, S. Gao, L. Wang, L. Wang, W. Wang, Difference of oxidation mechanism between light C3–C4 alkane and alkene over mullite YMn_2O_5 oxides catalyst, ACS Catal. 10 (2020) 7269–7282.
[58] J. Zhao, C. Tu, W. Sun, H. Xia, H. Zhang, Q. Dai, X. Wang, The catalytic combustion of CH_2Cl_2 over SO_4^{2-}–Ti_xSn_{1-x} modified with Ru, Catal. Sci. Technol. 10 (2020) 742–756.
[59] H. Wang, B. Peng, R. Zhang, H. Chen, Y. Wei, Synergies of Mn oxidative ability and ZSM-5 acidity for 1, 2-dichloroethane catalytic elimination, Appl. Catal. B 276 (2020) 118922.
[60] X. Lai, X. Zhou, H. Zhang, X. Jiang, T. Lin, Y. Chen, Toluene oxidation over monolithic MnO_x/La-Al_2O_3 catalyst prepared by a CTAB-assisted impregnation method, Appl. Surf. Sci. 526 (2020) 146714.
[61] L. Ma, C.Y. Seo, X. Chen, K. Sun, J.W. Schwank, Indium-doped Co_3O_4 nanorods for catalytic oxidation of CO and C_3H_6 towards diesel exhaust, Appl. Catal. B 222 (2018) 44–58.
[62] H. Kareem, S. Shan, Z.-P. Wu, L. Velasco, K. Moseman, C.P. O'Brien, D.T. Tran, I.C. Lee, Y. Maswadeh, L. Yang, D. Mott, J. Luo, V. Petkov, C.-J. Zhong, Catalytic oxidation of propane over palladium alloyed with gold: an assessment of the chemical and intermediate species, Catal. Sci. Technol. 8 (2018) 6228–6240.
[63] Z. Hu, X. Liu, D. Meng, Y. Guo, Y. Guo, G. Lu, Effect of ceria crystal plane on the physicochemical and catalytic properties of Pd/ceria for CO and propane oxidation, ACS Catal. 6 (2016) 2265–2279.
[64] H. Du, C.T. Williams, A.D. Ebner, J.A. Ritter, In situ FTIR spectroscopic analysis of carbonate transformations during adsorption and desorption of CO_2 in K-promoted HTlc, Chem. Mater. 22 (2010) 3519–3526.